

MERLIN observations of relativistic ejections from GRS 1915+105

R. P. Fender,^{1*} S. T. Garrington,² D. J. McKay,^{2,3} T. W. B. Muxlow,² G. G. Pooley,⁴
R. E. Spencer,² A. M. Stirling² and E. B. Waltman⁵

¹*Astronomical Institute ‘Anton Pannekoek’ and Center for High Energy Astrophysics, University of Amsterdam, Kruislaan 403, 1098 SJ Amsterdam, the Netherlands.*

²*University of Manchester, Nuffield Radio Astronomy Laboratories, Jodrell Bank, Cheshire, SK11 9DL*

³*Joint Institute for VLBI in Europe, Postbus 2, 7990 AA Dwingeloo, the Netherlands*

⁴*Mullard Radio Astronomy Observatory, Cavendish Laboratory, Madingley Road, Cambridge CB3 0HE*

⁵*Remote Sensing Division, Code 7210, Naval Research Laboratory, Washington, DC 20375-5351, USA*

Accepted 1998 December 8. Received 1998 December 3; in original form 1998 October 12

ABSTRACT

We present high-resolution MERLIN radio images of multiple relativistic ejections from GRS 1915+105 in 1997 October/November. The observations were made at a time of complex radio behaviour, corresponding to multiple optically thin outbursts and several days of rapid radio flux oscillations. This activity followed ~ 20 d of a plateau state of inverted-spectrum radio emission and hard, quasi-stable X-ray emission. The radio imaging resolved four major ejection events from the system. As previously reported from earlier VLA observations of the source, we observe apparent superluminal motions resulting from intrinsically relativistic motions of the ejecta. However, our measured proper motions are significantly greater than those observed on larger angular scales with the VLA. Under the assumption of an intrinsically symmetric ejection, we can place an upper limit on the distance to GRS 1915+105 of 11.2 ± 0.8 kpc. Solutions for the velocities unambiguously require a higher intrinsic speed by about $0.1c$ than that derived from the earlier VLA observations, whilst the angle to the line of sight is not found to be significantly different. At a distance of 11 kpc, we obtain solutions of $v = 0.98^{+0.02}_{-0.05}c$ and $\theta = 66^\circ \pm 2^\circ$. The jet also appears to be curved on a scale that corresponds to a period of around 7 d.

We observe significant evolution of the linear polarization of the approaching component, with large rotations in position angle and a general decrease in fractional polarization. This may be the result of increasing randomization of the magnetic field within the ejected component. We do not at any time detect significant linear polarization from the core, including periods when the flux density from this region is dominated by radio oscillations. The power input into the formation of the jet is very large, $\geq 10^{38}$ erg s⁻¹ at 11 kpc for a pair plasma. If the plasma contains a cold proton for each electron, then the mass outflow rate, $\geq 10^{18}$ g s⁻¹, is comparable to inflow rates previously derived from X-ray spectral fits.

Key words: accretion, accretion discs – stars: individual: GRS 1915+105 – stars: variables: other – ISM: jets and outflows – radio continuum: stars – X-rays: stars.

1 INTRODUCTION

GRS 1915+105 is a distant black-hole-candidate X-ray transient in the Galactic plane, discovered by the WATCH instrument on board the *GRANAT* mission in 1992 (Castro-Tirado, Brandt & Lund 1992). Owing to large extinction ($A_V \geq 20$ mag), the properties of the optical counterpart are unknown, but observations at radio, near-infrared and X-ray energies have shown GRS 1915+105 to be a highly unusual and energetic system.

Shortly after the discovery of the X-ray source, variable radio and infrared counterparts were identified (Mirabel et al. 1994). Subsequent mapping of the radio counterpart following an outburst in 1994 revealed apparent superluminal motions in a two-sided ejection of synchrotron-emitting components from the source (Mirabel & Rodríguez 1994, hereafter MR94). This was the first observation of superluminal motions in our Galaxy, the only previously measured proper motions of ejections from X-ray binaries (SS 433 & Cyg X-3) implying velocities of $\sim 0.3c$. Within a year, a second superluminal source, GRO J1655–40, had been discovered (Tingay et al. 1995; Hjellming & Rupen 1995).

*Email: rpf@astro.uva.nl

A third possible superluminal jet source, XTE J1748–288, has recently been reported (Rupen, Hjellming & Mioduszewski 1998).

The Very Large Array (VLA) observations of GRS 1915+105 by MR94 revealed proper motions of 17.6 ± 0.4 and 9.0 ± 0.1 mas d^{-1} for two components separating from a core at position angles of 150° and 330° , respectively. From H α absorption measurements these authors derived a most likely distance to the source of 12.5 ± 1.5 kpc, giving apparent transverse motions of $1.25c \pm 0.15c$ and $0.65c \pm 0.08c$, respectively. Proper motion and flux density ratios between the (inferred) approaching and receding components were consistent with simple ballistic bulk motions. Solving for the proper motions at a distance of 12.5 kpc, a true velocity of $0.92c \pm 0.08c$ at an angle of $70^\circ \pm 2^\circ$ to the line of sight was derived. Further observations with the VLA following a radio outburst in 1995 revealed relativistic ejection for a second time (Mirabel et al. 1996). However, the proper motions and flux density ratios appeared to be somewhat different from those reported in MR94 possibly implying a change in the jet velocity or the angle to the line of sight. A summary of multiple VLA observations of major relativistic ejections from GRS 1915+105 is given in Rodríguez & Mirabel (1999, hereafter RM99).

Pooley & Fender (1997, hereafter PF97) report ~ 2 yr of radio monitoring of GRS 1915+105 at 15 GHz with the Ryle Telescope (RT). They describe in detail quasi-periodic radio oscillations with periods typically in the range 20 – 40 min, a phenomenon not previously seen in any other source, and first reported in Pooley

(1995). Fender et al. (1997) report the discovery of infrared counterparts to the radio oscillations, suggesting an approximately flat synchrotron spectrum from cm to μm wavelengths. They proposed that each oscillation corresponds to a small ejection of material from the GRS 1915+105 system. Around the same time Belloni et al. (1997a,b) proposed that X-ray dips with similar periods correspond to the removal of the inner (≤ 200 km) region of the accretion disc, possibly advected into the black hole. The observation of a correlation between such X-ray dips and the rise of radio oscillations (PF97) seemed to complete a picture of repeated ejection and refill of the inner accretion disc, the ejecta emitting a flat synchrotron spectrum from 2 cm – $2 \mu m$ before they cool owing to adiabatic expansion losses. Further X-ray, radio and infrared timing observations (Eikenberry et al. 1998; Mirabel et al. 1998; Fender & Pooley 1998) appear to confirm this model, at least qualitatively.

Long-term comparison of radio and 2–12 keV X-ray light curves in PF97 revealed an unusual period of activity in 1996 July–August, hereafter the ‘plateau’ state, during which time the X-ray emission entered a hard, quasi-stable state, while the radio emission became relatively bright at 15 GHz. Earlier occurrences of this state are reported in Foster et al. (1996) and Harmon et al. (1997). Bandyopadhyay et al. (1998) also discuss bright infrared emission during such periods. It was speculated in PF97 (and earlier, in Harmon et al. 1997) that such plateau states may correspond to major radio ejections from the GRS 1915+105 system. Fig. 1 shows that a

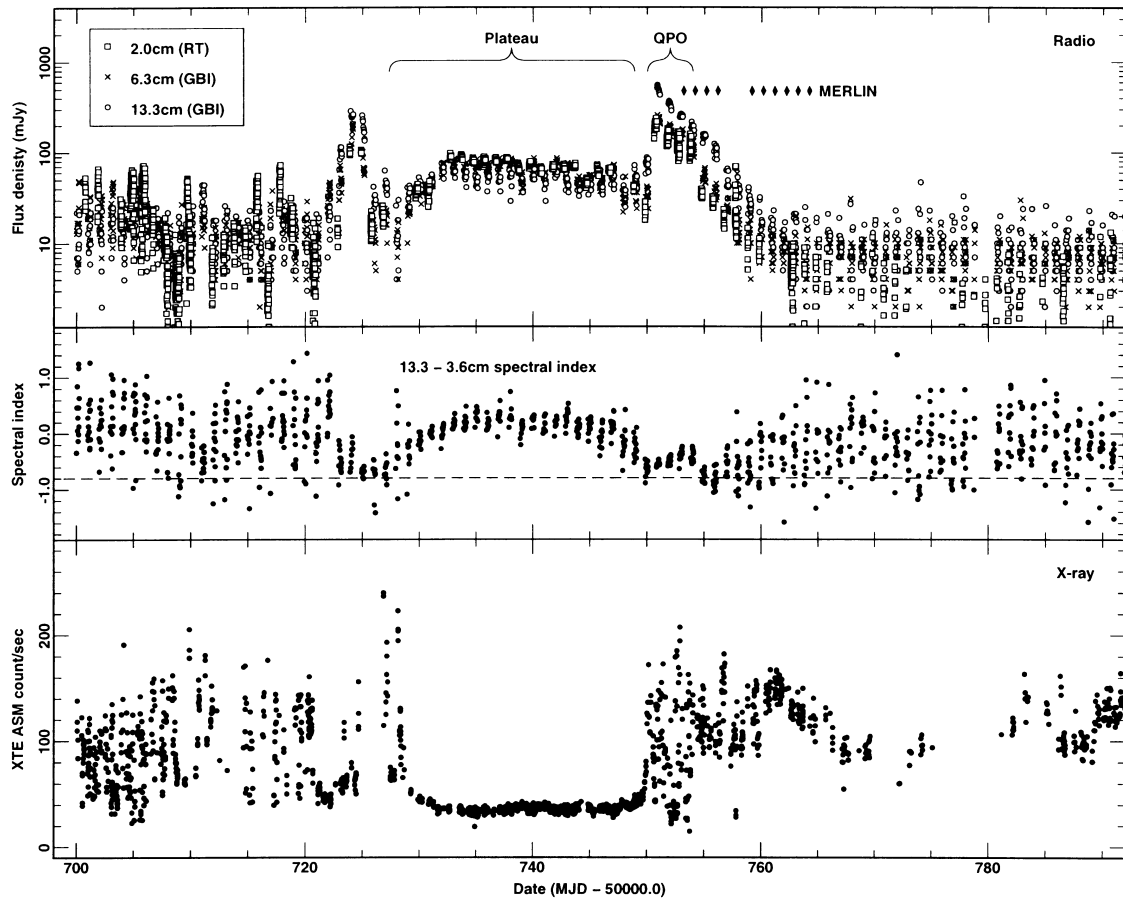


Figure 1. Radio and X-ray flux monitoring spanning the sequence of radio ejections mapped by MERLIN. The upper panel shows the flux densities measured at 2.0 cm with the RT, and at 6.3 cm and 13.3 cm with the GBI. The middle panel shows the radio spectral index from simultaneous measurements at 13.3 and 3.6 cm. The lower panel shows the count rate in the 2–12 keV band by the *Ross X-ray Timing Explorer* (RXTE) All-Sky Monitor (ASM). The optically thin state evolves towards a spectral index of -0.8 , which is shown by the dashed line in the middle panel.

significant radio flare occurred around MJD 50725. This was the prelude to a plateau state lasting 20 d in which a bright, apparently optically thick, radio source was formed, coinciding with a quasi-stable, hard X-ray state. At the end of the plateau stage a second, major radio flare occurred, which triggered the multi-element radio-linked interferometer network (MERLIN) mapping observations, the highest resolution imaging of GRS 1915+105 to date. Each MERLIN map epoch is indicated by a diamond in the upper panel of Fig. 1.

2 OBSERVATIONS

2.1 MERLIN

GRS 1915+105 was observed using the MERLIN array at 4.994 GHz with a bandwidth of 16 MHz. MERLIN is comprised of six individual antennas, typically 25 m in diameter and with a maximum separation of 217 km. 10 imaging runs were made as a target-of-opportunity programme triggered by flux monitoring at the RT and Green Bank Interferometer (GBI), showing the source had flared to around 250 mJy at 2–15 GHz. MERLIN, by default, samples both left-hand and right-hand polarizations allowing the full range of Stokes parameters to be imaged. Details of the observations can be found in the Table 1, and continuum and polarization maps in Figs 2 and 3, respectively.

Each separate epoch includes observations of a flux and polarization angle calibrator, 3C286, a point-source calibrator, OQ208 or 0552+398, the compact phase reference source, 1919+086 and the target GRS 1915+105. By nodding the array to the phase reference source, the interpolated phase variations owing to atmospheric density variations were removed from the target source data. The nodding cycle of 8 min on the target and 2 min on the reference source reflects the phase stability of MERLIN at this frequency.

Phase referencing allows the registration of individual images to around 10 mas, given the changeable weather conditions during the observations. The absolute positions are tied to the radio reference frame (ICRF) using the calibrator 1919+086, the position of which is known to around 17 mas relative to that frame (Patnaik et al. 1992).

Using the MERLIN d-programs, initial data editing and amplitude calibration were performed and the data prepared for further reduction in the National Radio Astronomy Observatories' (NRAO) AIPS package. After further editing in AIPS, each data set was run through the MERLIN pipeline, which images the phase reference

source and applies the derived corrections. Instrumental polarization corrections were made using 1919+086 and the polarization position angles were calibrated using 3C286, for which a position angle of 33° for the E vector of linear polarization was assumed.

Subsequent self-calibration using the phase reference images as starting models was straightforward. Imaging the Stokes parameters I , Q and U using the AIPS task IMAGR gives the final total intensity contour maps with superimposed vectors representing linearly polarized intensity. All the images have been restored with a 40-mas [full width at half-maximum (FWHM)] circular beam.

All the maps are affected to some degree by the variations in source structure and brightness during the observations. In 12 h, the source expands by (typically) one-quarter of a beamwidth, and during the first four epochs the flux-density changes were as much as 10 per cent over each individual epoch. Although these two effects are difficult to disentangle, and we are in the process of simulating such changes to quantify their magnitude, we believe that there will be no serious consequences for the images beyond increased uncertainties in the positions of components, at the level of a few mas, and the presence of sidelobes around bright components (at a few per cent of the peak brightness) in the maps at early epochs.

Relative positions of components were found by measuring radial distances of the components from a nominal map centre. RMS errors in this process are estimated to be 6 mas, degrading to 15 mas for the weaker components in the later epochs. The error in the absolute position of each component is ~ 22 mas.

A montage of all 10 epochs is presented in Fig. 2. At least four approaching (SE, C1, C2, C3) components and one receding (NW) component are clearly resolved. The receding component corresponding to ejection C1 may be also resolved in the last three epochs (less likely, but possible, is a physical splitting of component NW). The maps have been rotated clockwise by 52° , so that the mean position angle of the jet on the sky is 142° .

2.2 Ryle Telescope

The source was monitored at 15 GHz using the RT at Cambridge. At least a short observation was possible on most days during this period. The details of the observing technique are as given in PF97. The data, in 5-min bins, are plotted in the top panel of Fig. 1. Data sampled at 32-s intervals are shown in Fig. 4 for the rapid (oscillation) variations observed at four epochs.

Table 1. Measured quantities from MERLIN maps: angular separation (mas) from the core, flux densities (mJy), and fraction of linear polarization for all well-resolved components. SE and NW correspond to the approaching and receding components of the first major ejection. C1 – C3 are subsequent approaching ejections. $M = P/I$ is the fractional linear polarization, where measurable. The errors in fractional polarization are typically 0.01 except for the last epoch quoted where they may reach 0.04 for the weaker NW component.

MJD	Total flux	SE		M	NW		M	C1		C2		C3		Typical errors	
–50000.0	density	Posn	Flux	P/I	Posn	Flux	P/I	Posn	Flux	Posn	Flux	Posn	Flux	Flux	Posn
752.71	179.8	46	79.9	0.14	15	109.7	< 0.03							0.4	6
753.71	139.9	69	48.3	0.08	23	93.9	< 0.03							0.3	6
754.70	85.2	99	46.3	0.06	31	17.9	0.10	38	25.9					0.3	6
755.70	63.6	122	31.0	0.06	46	11.7	0.13	31	21.4					0.2	6
758.68	16.4	191	4.8		84	4.8		92	2.9	6	3.8			0.2	8
759.68	12.2	206	2.0		99	3.1		130	2.7	76	4.6			0.1	10
760.68	7.1	237	1.8		99	2.4				106	2.3			0.1	10
761.72	7.4	252	0.6		107	1.8		206	0.6	137	1.5	69	1.6	0.1	15
762.72	6.4	279	0.4		113	1.4		211	1.1	151	1.1	83	1.1	0.1	15
763.72	3.6	317	0.3		136	0.9		242	0.4	158	0.5	98	0.9	0.1	15

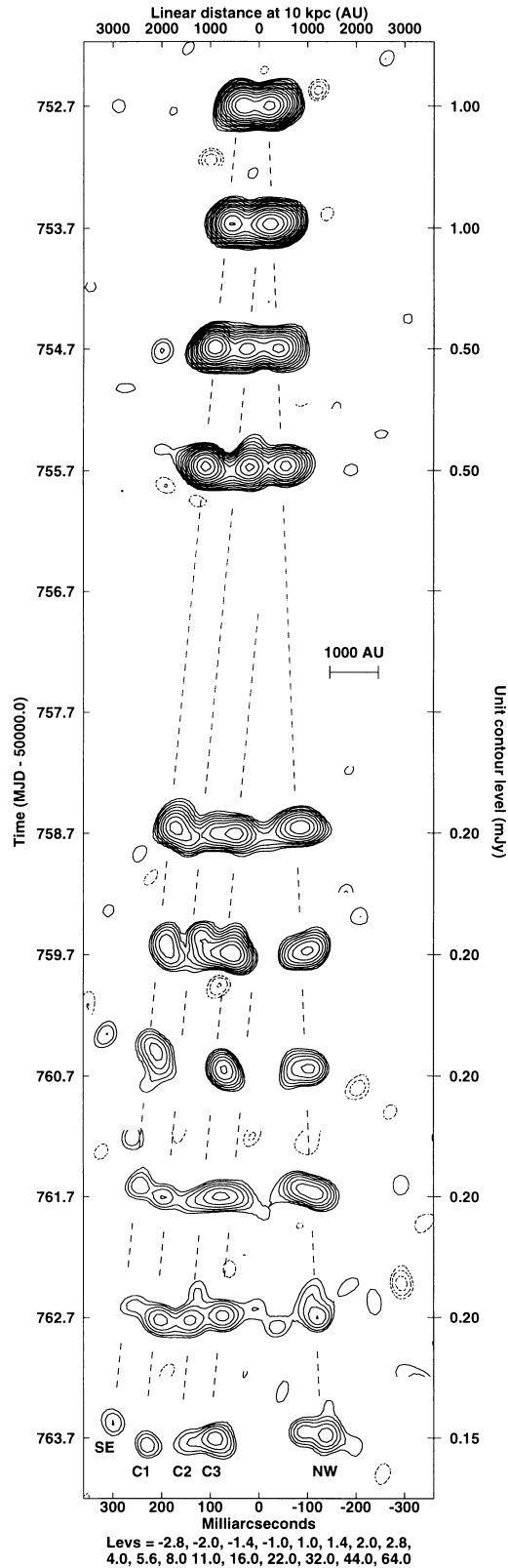


Figure 2. MERLIN maps of total intensity from 10 – 12 h observations at the epochs illustrated on Fig. 1. The images have been rotated clockwise by 52° to form the montage. Contour levels increase in factors of $\sqrt{2}$ from the unit contour level indicated at the right-hand side of each image. Mapping fidelity is dominated by dynamic range considerations for the first five epochs, whilst receiver noise dominates later.

2.3 Green Bank Interferometer

GRS1915+105 was monitored at 2.25 and 8.3 GHz throughout 1997 using the two-element GBI. The observing and calibration procedures were the same as described by Foster et al. (1996). Random errors for the GBI are flux-density dependent, approximately (one sigma) 4 mJy at 2 GHz and 6 mJy at 8 GHz for fluxes < 100 mJy; 8 mJy at 2 GHz and 25 mJy at 8 GHz for fluxes near 0.5 Jy. We estimate that systematic errors may approach 10 per cent at 2 GHz and >20 per cent at 8 GHz. Fig. 1 displays the GBI data at 2 and 8 GHz during MJD 50700–50800 and exhibits both plateau (50730–50750) and flaring (50721–50725 and 50750–50756) behaviour as described by Foster et al. (1996).

It should be noted that the *plateau* state discussed in this paper is consistent with the definition in Foster et al. (1996) but that our definition, i.e. flat-spectrum radio emission at about 100 mJy at the same time as quasi-stable X-ray emission with a significant hardening of the spectrum, may be more specific.

2.4 RXTE

The target is monitored up to several times daily in the 2–12 keV band by the *Rossi X-ray Timing Explorer* (RXTE) All-Sky Monitor (ASM). See e.g. Levine et al. (1996) for more details. The total flux measured by individual scans is plotted in the bottom panels of Figs 1 and 4.

3 SUPERLUMINAL EJECTIONS

Fig. 2 presents the 10 MERLIN maps of GRS 1915+105. The images clearly show expansion of the source, with components on the left-hand side (south-east – maps have been rotated clockwise by 52°) appearing to move faster. The two components just resolved in the first image can be followed through all epochs as they move out and their brightness declines. We label these components SE and NW. Further components can be seen to be ejected later and are labelled C1, C2 and C3. The proper motions of the components are consistent with ballistic motions, and so we can extrapolate back to derive their times of formation (see Fig. 5). We estimate these to be as follows (in MJD):

$$\text{NW} + \text{SE} : 50750.5^{+0.08}_{-0.2}$$

$$\text{C1} : 50753.5 \pm 0.8$$

$$\text{C2} : 50756.6 \pm 1.6$$

$$\text{C3} : 50758.0 \pm 2.0.$$

The latest time of the NW+SE ejection is constrained by the observation of core-dominated radio oscillations by MJD 50750.58 (Fig. 4), as well as uncertainties in the model fits. The individual components are unresolved in the first four epochs. There is some evidence of them becoming resolved or breaking up into subcomponents in the latest three epochs. Epochs 5, 6, 7 and 9 show that there is some emission between the knots, which may indicate the presence of an underlying continuous jet. However, given the possible problems of varying flux density and structure through the observations and the low signal-to-noise ratio in the later epochs, we cannot be certain about some of these features. The possible bending of the jet will be discussed briefly below.

We will concentrate our quantitative analysis on those components that can be followed through three or more epochs. The rapidly outflowing components are generally moving faster, and

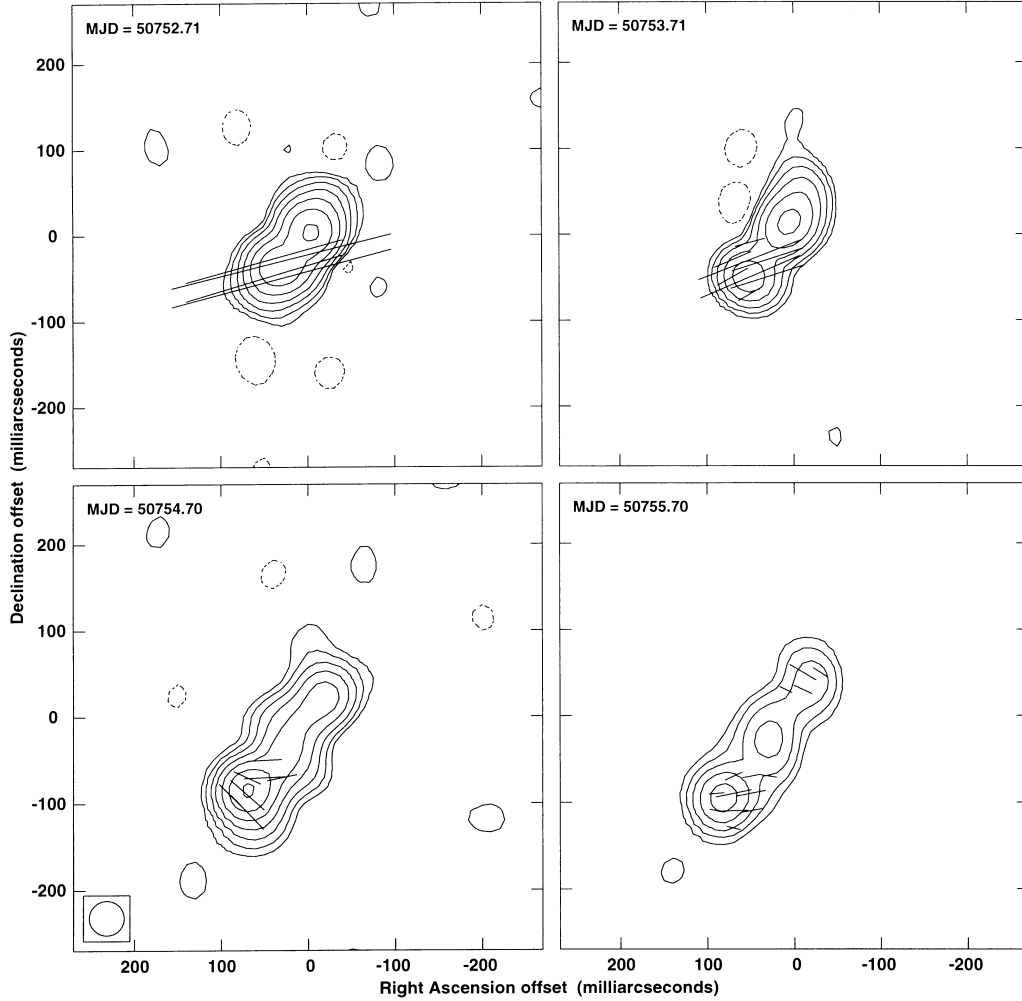


Figure 3. Linear polarization E vectors superimposed upon total intensity contour maps of the first four epochs of MERLIN observations. For polarization vectors, $100 \text{ mas} = 3.33 \text{ mJy beam}^{-1}$. This clearly shows the depolarization of the core and receding components with respect to the approaching component, and the rotation of polarization vectors in the approaching component.

brighter, on the SE side. (Note that the apparent high brightness of the NW component in the second epoch is due to a blend with the core.)

From these components we can measure proper motions, flux densities and (in some cases) polarizations. These we deal with quantitatively below.

3.1 Proper motions

An examination of the positions of the components shows an apparent expansion velocity at greater than $2c$, thus relativistic effects are important. As a result the approaching components will have a higher apparent motion than that of the receding components. The component to the NW clearly has the lowest apparent speed so we therefore identify it as receding; there are three components to the SE that we identify as approaching. The data are best fitted by proper motions of

$$\mu_{\text{app}} = 23.6 \pm 0.5 \text{ mas d}^{-1}$$

and

$$\mu_{\text{rec}} = 10.0 \pm 0.5 \text{ mas d}^{-1}.$$

All fits are good, with $\chi^2_{\text{red}} \leq 1$, and illustrated in Fig. 5. The proper

motion of $17.6 \pm 0.4 \text{ mas d}^{-1}$ reported by MR94 for the approaching component can be ruled out; fixing the proper motion to this value does not give an acceptable fit to the data.

Following the method of MR94, *under the assumption of an intrinsically symmetric ejection*, we can derive

$$\beta \cos \theta = \frac{\mu_{\text{app}} - \mu_{\text{rec}}}{\mu_{\text{app}} + \mu_{\text{rec}}} = 0.41 \pm 0.02, \quad (1)$$

where β is the velocity of the ejections expressed as a fraction of the speed of light, and θ is the angle between the ejection and the line of sight. This immediately gives us a maximum angle to the line of sight (setting $\beta = 1$) of $\theta_{\text{max}} \leq 66^\circ \pm 2^\circ$, and a minimum velocity (setting $\cos \theta = 1$) of $\beta_{\text{min}} \geq 0.41 \pm 0.02$.

A maximum distance to GRS 1915+105 can also be inferred for a maximum possible velocity of the ejecta of $\beta = 1$

$$d_{\text{max}} \leq \frac{c \tan \theta_{\text{max}} (\mu_{\text{app}} - \mu_{\text{rec}})}{2 \mu_{\text{app}} \mu_{\text{rec}}}, \quad (2)$$

which can be expressed in convenient units as

$$d_{\text{max}} \leq 87 \tan \theta_{\text{max}} \left(\frac{\mu_{\text{app}} - \mu_{\text{rec}}}{\mu_{\text{app}} \mu_{\text{rec}}} \right) \text{ kpc} \quad (3)$$

(for μ_{app} and μ_{rec} in mas d^{-1}). The proper motions observed with

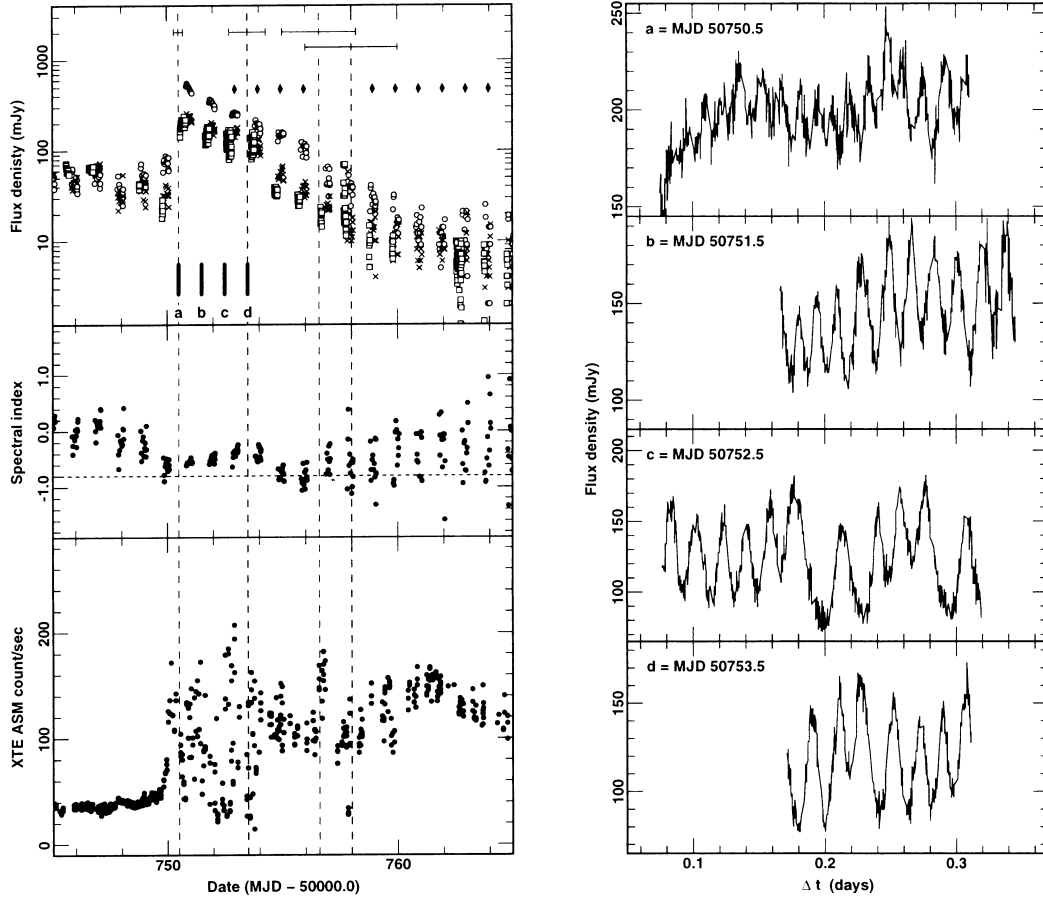


Figure 4. A detailed view of the radio and X-ray behaviour of GRS 1915+105 during the ejection episode. Symbols are as shown in Fig. 1. The vertical dotted lines, with error bars, indicate our derived times for the beginning of each of the four ejections. The four solid vertical bars labelled a–d drawn on the top left radio monitoring panel between the first and second ejections, indicate the four periods of 15-GHz monitoring highlighted in the panels on the right. The source appears to exhibit continuous short period (20–40 min) oscillations in this phase, indicative of repeated advection or ejection and refill of the inner accretion disc. The radio QPO do not repeat after the second ejection, but there are some indicators of the second and third ejections in the X-ray data.

MERLIN therefore constrain the maximum distance to be 11.2 ± 0.8 kpc. MR94 state that GRS 1915+105 must be further than the H II region G45.45+0.06 (mistyped by them as G45.46+0.06; Downes et al. 1980) based upon their H I spectral observations. While MR94 state that this H II region lies at ~ 8.8 kpc, in a recent study Feldt et al. (1998) adopt a distance of 6.6 kpc, and so GRS 1915+105 appears to lie at a distance of between 7 – 12 kpc, significantly closer than previously thought. Given the high observed H I column density to the source, from which MR94 inferred a large distance of 12.5 ± 1.5 kpc, we adopt a value of 11 kpc for the distance to GRS 1915+105.

We can solve for the angle to line of sight and velocity, for any distance to GRS 1915+105. The angle to the line of sight

$$\theta = \tan^{-1} \left[1.16 \times 10^{-2} \left(\frac{\mu_{\text{app}} \mu_{\text{rec}}}{\mu_{\text{app}} - \mu_{\text{rec}}} \right) d \right], \quad (4)$$

where d is the distance to the source in kpc, and μ_{app} and μ_{rec} are in mas d^{-1} . Once θ is calculated, we can immediately derive β as the value of $\beta \cos \theta$ is already known.

Table 2 lists the apparent velocities and solutions for the angle to the line of sight and intrinsic velocities for both these MERLIN observations and the VLA observations of MR94, for assumed distances of 9, 10, 11 and 12 kpc. Fig. 6 shows these solutions for all distances between 7 – 12 kpc. Our MERLIN data unequivocally

imply a higher intrinsic velocity, by $\Delta\beta \sim 0.1$, in comparison with the observations reported in MR94.

3.2 Flux densities and ratios

The ratio of flux densities from the approaching and receding components is another important diagnostic of the ejections. In the above calculations we have assumed geometric symmetry; here we also assume that the jet components on both sides have the same intrinsic luminosity (which does not appear to be the case for GRO J1655-40; Hjellming & Rupen 1995). When measured at equal angular separations from the core (i.e. the same time since ejection in the rest frame of the ejecta) and coupled with the observed spectral index we can test the theoretical predictions for Doppler (de)boosting of the components.

The mean spectral index of the ejecta is hard to determine owing to both overlapping ejection events and the presence of rapid flat-spectrum oscillations from the core (PF97 and below). Our best estimate for the index, defined as $\alpha = \Delta \log S_\nu / \Delta \log \nu$ is around -0.8 , the same as reported by MR94. This is determined primarily from the simultaneous Green Bank monitoring at 13.3 and 3.6 cm and should be a good estimate for the 6-cm MERLIN observations. It is difficult to measure accurately the ratio of flux densities of the components at equal angular separations, given their very different

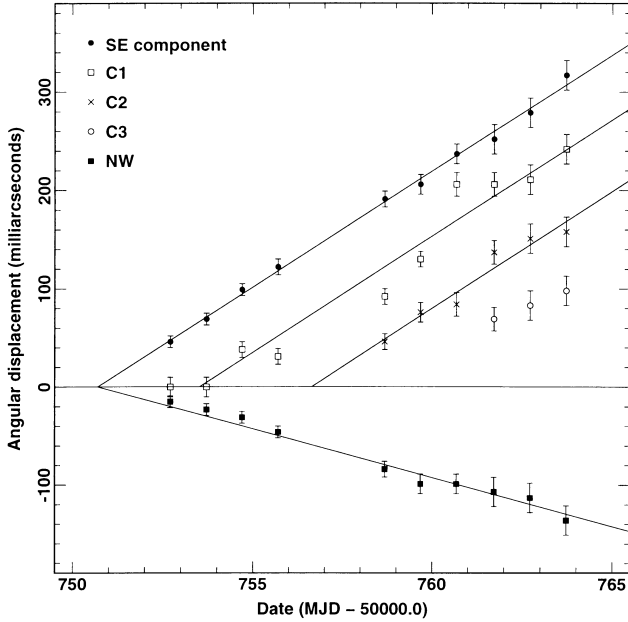


Figure 5. Angular separation as a function of time for approaching components SE, C1, C2 and C3 and receding component NW. All approaching components are consistent with unaccelerated proper motions of $23.6 \pm 0.5 \text{ mas d}^{-1}$, significantly faster than those reported in MR94. The receding component, NW, has a proper motion of $10.0 \pm 0.5 \text{ mas d}^{-1}$, and corresponds to the same ejection epoch as SE, on MJD $50750.5^{+0.08}_{-0.2}$.

proper motions, but it lies between 6 and 10. This is compatible with the 8 ± 1 reported in MR94.

For bulk motions at velocity β the observed ratio is predicted to be

$$\frac{S_{\text{app}}}{S_{\text{rec}}} = \left(\frac{1 + \beta \cos \theta}{1 - \beta \cos \theta} \right)^{k-\alpha}, \quad (5)$$

where, theoretically, $k = 2$ for continuous jets and 3 for discrete components. As $\beta \cos \theta$ is already calculated as 0.41 ± 0.02 , and independent of distance, we can solve for k . For a flux density ratio in the range 6 – 10, $k = 1.3 - 1.9$. As in MR94, the flux ratio appears to be closer to that expected for a continuous jet than for discrete components (although the value derived from the data of MR94 is $k = 2.3$, interpreted by them as implying something intermediate between a continuous jet and discrete ejections). For $k = 3$ we would have expected a flux ratio of ~ 27 .

Fig. 7 shows the flux density of each well-observed component as a function of angular separation from the core. As is obvious from Table 1 and the maps of Fig. 2, the ejections in the sequence

NW+SE, C1, C2, C3 are of steadily decreasing flux density. While uncertainties in both flux density and position make interpretation difficult, the data do not appear to show the straight-line behaviour expected for a power-law decay (for the case of adiabatic expansion losses and a constant expansion rate). Exponential fits to the data provide no improvement. RM99 discuss a steepening of the decay of the radio flux density at an angular separation of ~ 1 arcsec; as we only image on smaller scales we cannot test this. Atayan & Aharonian (1997) discuss the implications of the flux ratio in considerable detail.

3.3 Polarization

Polarisation images have been made for the first four epochs, when the source was sufficiently bright to detect linear polarization at the level of a few per cent. These are shown in Fig. 3, where the vectors represent the fractional linear polarization and observed electric field angle. The fractional linear polarizations are also listed in Table 1. No circular polarization was detected at any time, with a conservative upper limit of 2 per cent.

3.3.1 Resolved ejecta

The images of the ejected components show a striking asymmetry in the linear polarization – only the approaching SE component appears significantly polarized. Its fractional polarization decreases rapidly from 14 to 6 per cent, and the polarization position angle swings by approximately 75° between the second and third epochs, then swings back by 45° . In the fourth epoch image, there is marginal detection of polarized emission in the receding NW component, at a level of 13 ± 5 per cent.

The changes in polarization seen in the MERLIN images could be a result of changing Faraday effects (internal or external) or changing magnetic field geometry within the radio components. With only a single frequency it is hard to distinguish between these possibilities. If the observed change in position angle is due to Faraday rotation, the implied change in rotation measure is $> 300 \text{ rad m}^{-2}$.

The radio components are believed to be considerably denser than their surroundings (observed limits on the deceleration imply a density contrast of at least 10) and have equipartition field strengths of order 50 mG (see below), presumably much greater than in the surrounding medium. The Faraday depth, or rotation measure, is proportional to $nB(Ld)^{1/2}$, where n is the thermal electron density, B is the magnetic field strength, L is the path length and d is the field tangling scale. The Faraday depth within the source is therefore likely to exceed the Faraday depth of a surrounding medium distributed on a scale size comparable to the source itself. As the components expand, their internal Faraday depths will fall, and any

Table 2. Apparent velocities, solutions for the angle to the line of sight, intrinsic velocity of ejection (assuming symmetry), and bulk motion Lorentz factors for values of proper motion measured by MERLIN and previously by the VLA (MR94), for assumed distances of 9, 10, 11 and 12 kpc. The functions are plotted in full, with consideration of measurement errors, in Fig. 6.

Distance (kpc)	Apparent velocity				Angle to line of sight		Intrinsic velocity		Bulk motion Lorentz factor	
	(appr.)	(reced.)								
	MERLIN	VLA	MERLIN	VLA	MERLIN	VLA	MERLIN	VLA	MERLIN	VLA
9	1.2 <i>c</i>	0.93 <i>c</i>	0.53 <i>c</i>	0.48 <i>c</i>	62°	63°	0.84 <i>c</i>	0.71 <i>c</i>	1.8	1.4
10	1.4 <i>c</i>	1.1 <i>c</i>	0.59 <i>c</i>	0.55 <i>c</i>	64°	66°	0.92 <i>c</i>	0.79 <i>c</i>	2.6	1.6
11	1.5 <i>c</i>	1.2 <i>c</i>	0.64 <i>c</i>	0.60 <i>c</i>	66°	68°	0.98 <i>c</i>	0.86 <i>c</i>	5.0	2.0
12	1.5 <i>c</i>	1.2 <i>c</i>	0.66 <i>c</i>	0.63 <i>c</i>	68°	69°	1.01 <i>c</i>	0.89 <i>c</i>	—	2.2

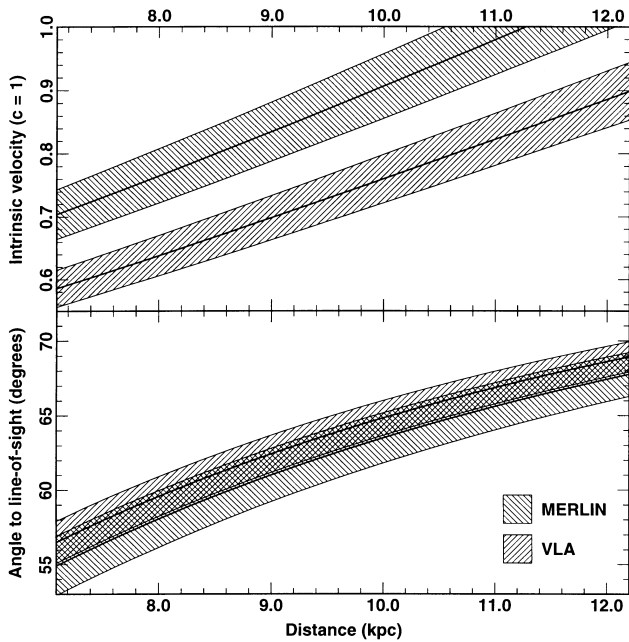


Figure 6. Derived intrinsic velocities and angles to the line of sight for MERLIN and VLA observations, under the assumption of intrinsically symmetric ejections. Solutions are possible for the same angle to the line of sight during both sets of observations, but the velocity derived for the MERLIN observations is higher than that for the VLA observations, by $\Delta\beta \sim 0.1$.

internal Faraday depolarization would decrease. This is contrary to the observed decrease in fractional polarization. Therefore, we do not believe the changes in polarization are due to changing Faraday depths, and this is consistent with the low rotation measure observed by Rodríguez et al. (1995).

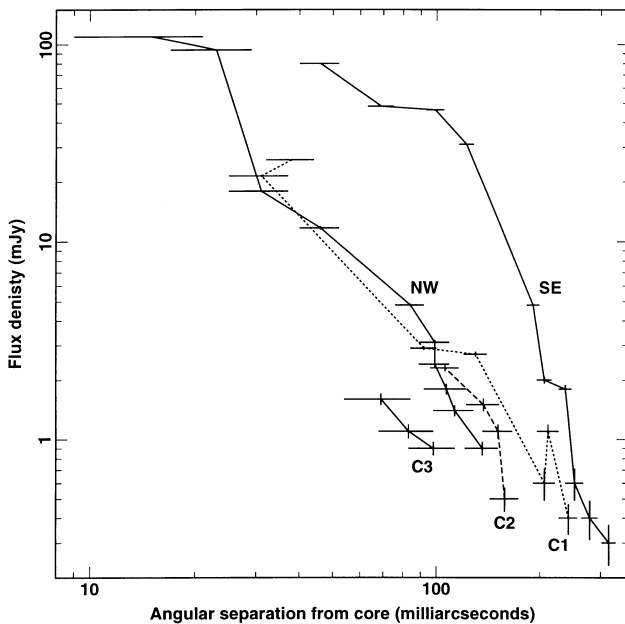


Figure 7. Flux densities of individually resolved components as a function of angular separation from the core. Simple power-law and exponential decay models do not fit the data well. The flux density ratio of SE : NW, approaching and receding components from the same ejection, ranges from 6 – 10.

Rodríguez et al. (1995) noted a fractional polarization of approximately 2 per cent at 5.0, 8.4 and 15 GHz at a position angle of $178^\circ \pm 10^\circ$ on 1994 March 24, when the source was barely resolved by the VLA and 5 d after the radio components were ejected. At this time the emission was probably dominated by the approaching component. The similarity of the fractional polarization and position angle at the three wavelengths implies that Faraday effects were small at 5.0 GHz. The implied upper limit to the Faraday rotation measure is 50 rad m^{-2} .

Superluminal jets in active galactic nuclei (AGN) often show complex radio polarization behaviour: rapid variations in polarization position angle (e.g. 0917+624 for an extreme case, Quirrenbach et al. 1989) and small-scale variations along the jet (e.g. 3C454.3, Kemball, Diamond & Pauliny-Toth 1996). This is usually interpreted as being the result of shocks, which compress and order the magnetic field (Cawthorne et al. 1993), and which appear as radio knots in an otherwise continuous jet.

The radio components of GRS1915+105, on the other hand, are thought to be discrete plasmons, rather than features (shocks or otherwise) in a continuous jet. In this case the changes in radio polarization indicate changes in the internal magnetic field geometry, such as randomization of the magnetic field as the plasmons evolve. The effects of aberration on a planar structure such as a shock would result in the two components having different observed polarization characteristics. However, the low signal-to-noise for the measurement of polarization in the receding component does not allow us to make such a distinction in this case.

3.3.2 Core

The core, sometimes blended in our images with newly formed major ejections, does not at any time show significant linear polarization. In particular, during the first two epochs of observation, the core is dominated by the flat spectrum oscillations of the type discussed in detail in PF97 (see Fig. 4). The lack of observed polarization may be the result of superposition of multiple components with different polarization position angles within the beam, or large Faraday depths close to the binary system (either internal to the compact base of the jet or in the form of circumstellar material).

3.4 An underlying curved jet?

In several of the MERLIN maps there is a hint of extended emission between the components. Furthermore, the low value of k derived from the flux-density ratios and $\beta \cos \theta$ is more consistent with a continuous jet than physically discrete components (see above). In addition, the jet appears to be curved, an effect that may also be marginally apparent on reinspection of the VLA images of MR94.

First, comparing the flux in discrete components in the MERLIN maps with respect to radio monitoring with GBI and RT (in which the source and jets will be unresolved), we find that the values agree to within a few per cent. So the overwhelming majority of the synchrotron emission, at cm wavelengths at least, arises in unresolved (with MERLIN) bright spots. On the other hand, we both derive (Section 3.2) and apply (Section 4.1) $k \sim 2$, the value theoretically expected for a continuous jet. We must conclude that the data are not good enough at present to establish definitively whether the ejections are in discrete components or we are observing the bright parts of a continuous jet. In the latter case, we can at least now state that any underlying continuous jet is very faint and less than a few mJy at cm wavelengths.

The possible curvature of the jet is not addressed quantitatively here, but we do believe this effect to be real. Discrimination between ballistic and helical effects, the latter possibly the result of Kelvin–Helmholtz instabilities, is not possible at this stage. The ‘period’ of any bending observed at angular scales imaged with MERLIN is around 7 d. It is interesting to note that the ‘period’ of the jet bending in GRO J1655–40 reported by Hjellming & Rupen (1995) of 3.0 ± 0.2 d turned out to be very close to the subsequently discovered orbital period of 2.6 d (Bailyn et al. 1995). We are confident that the apparent bending is not due to the rapid angular and flux-density evolution of the source during a 12-h observation (c.f. however, very long baseline interferometry (VLBI) observations of GRO J1655–40, Tingay et al. 1995, where both higher proper motions and finer angular resolution exacerbated the effect).

3.5 Collimation and expansion of components

From the lack of clearly resolved structure perpendicular to the jet axis at the 40 mas resolution of MERLIN, we can place constraints on the opening angle and lateral expansion of the ejected components. The maximum distance from the core that we track ejected components is ~ 300 mas, and this constrains the opening angle of the jet to $\leq 8^\circ$ over distances from the core ≤ 4000 au (6×10^{16} cm). Similarly, the ratio of lateral expansion to forward velocities is constrained to be ≤ 0.14 , i.e. a maximum lateral expansion velocity $\leq 0.14c$ (for jet bulk velocity of c).

4 DISCUSSION

4.1 Energetics and mass flow

4.1.1 Estimation of the internal energies of the jet components

Initially, we must work in the rest frame of the emission region. Converting the observed parameters (emission frequency, luminosity etc.) requires the value of the bulk Lorentz factor γ , which is somewhat uncertain as discussed in Section 3.1, on account of the uncertainty in the distance. Because of the large angle to the line of sight, the Doppler factors for both the approaching and receding components,

$$\delta_{\text{app,rec}} = \gamma^{-1}(1 \mp \beta \cos \theta)^{-1} \quad (6)$$

are both less than unity for the range of Lorentz factors considered here.

The estimation of the parameters of the synchrotron emission region is detailed by Longair (1994) and Hughes (1991). We adopt the formulae in the summary by Longair (allowing for the opposite convention for the sign of α). These include a number of simplifying assumptions that are unlikely to introduce larger uncertainties than those imposed by our imperfect knowledge of the source parameters.

In order to estimate the internal energy of the emitting component, we need to know the synchrotron spectrum and the source geometry. A radio spectrum of the form $S \propto \nu^\alpha$ arises from an electron population with an energy spectrum $N(E) \propto E^{-(1-2\alpha)}$. The observed luminosity can arise from various combinations of magnetic flux density B and particle density, both of which we assume to be spatially uniform; the total energy is minimized to derive the ‘minimum energy’ conditions: the total energy in relativistic electrons, and the misleadingly named B_{min} , the field at which the total energy is minimized. As is well known, the minimum energy result nearly coincides with equal energies in magnetic field and particles, or equipartition. There are physical plausibility arguments for such a situation, but very few measurements that confirm that

this situation might actually pertain to any particular case (see Harris, Carilli & Perley 1994 for data on the radio galaxy Cygnus A, which suggest, in that case, that conditions may be near to those suggested by this method).

The calculation can easily be adapted to include a contribution to the energy by a hypothetical population of relativistic protons, which do not radiate significantly by the synchrotron mechanism if their energies are comparable with those of the electrons.

If the energy spectrum of the electrons is relatively steep (α steeper than -0.5), as in this case, the total energy of the particles is dominated by the lower end of the distribution. The lowest frequency detected, and the luminosity at that frequency, are then parameters in the calculations.

The source geometry is, so far, not well-defined. Direct observations only give an upper limit to most dimensions: the resolution of MERLIN is 50 mas, corresponding to 8×10^{13} m, or 3 light days, at 11 kpc. We have to rely on the time-scale of the variations in flux density for a better limit; the rise times are the shortest and therefore most restrictive. The rise times may represent the interval during which relativistic material is injected, or alternatively a transition in optical depth (or both). We believe that the former (injection time-scale) is most likely to be the dominant effect, as the spectral data suggest that the source is optically thin as soon as the jet is visible.

As the rise time for the jet components appears to be less than 12 h, we adopt 12 light-h (1.3×10^{13} m) as a ‘typical’ size on formation of the jet component. In comparison, RM99 discuss a geometric mean angular size of 35 mas, corresponding to a linear scale of 6×10^{13} m. We stress the weak links in this argument, elaborated by Longair (1994) and Hughes (1991):

- (i) We have only rather weak constraints on the source size, and certainly do not know the filling factor of the source, and this is one of the major uncertainties in the calculation. A smaller size or filling factor reduces the total energy required as $(\text{volume})^{3/7}$.
- (ii) There is little evidence that the minimum-energy condition is achieved.
- (iii) The contribution of protons (and other nuclei) is not known.
- (iv) The limits on the energy spectrum are not well-defined by current observations.

We now apply the formulae from Longair (1994); his equations (19.29) and (19.30), using the following measured, estimated or derived parameters:

- (i) adopted distance 11 kpc;
- (ii) $\gamma = 5.0$ (see Table 2);
- (iii) $\beta \cos \theta = 0.41$;
- (iv) spectral index $\alpha = -0.8$;
- (v) Doppler factors $\delta_{\text{app,rec}} = \gamma^{-1}(1 \mp \beta \cos \theta)^{-1} = 0.34, 0.14$;
- (vi) $k = 2$ (Section 3.2);
- (vii) ratio of relativistic proton energy to electron energy, $(\eta - 1) = 0$;
- (viii) total source volume $V = 10^{39} \text{ m}^3$;
- (ix) monochromatic luminosity L_ν , in the rest frame, at the lowest frequency detected, as derived below.

The maximum observed flux density observed at the start of the outburst at 2.3 GHz is 550 mJy (Fig. 4), some 2 d before the first MERLIN map. This would correspond to 1 Jy at 1 GHz, assuming the spectral index to be -0.8 . We adopt 1 GHz as the lowest frequency at which emission was detected during this outburst (Hannikainen & Hunstead, private communication, detected the outburst at 843 MHz). We assume that this flux density is dominated by the approaching component. Its apparent flux density if observed

Table 3. A summary of the derived properties of the ejecta at minimum energy conditions, calculated for a distance of 11 kpc, and summing both sides of the ejection. We assume that radio emission observed by GBI and RT at the peak of the flare are dominated by the approaching (SE) component, and take 1 and 15 GHz as upper and lower bounds of the observed flaring emission respectively. We assume a generation time for the ejection of 12 h. Proton mass and mass flow rate are for the case of 1 proton for each electron.

Minimum energy condition				Ejecta		Power	Mass outflow
E_{\min} (erg)	$E_{K,\min}$	B_{\min} (mG)	N_e	$M_e(\text{rest})$ (g)	M_p (g)	(erg s ⁻¹)	rate (g s ⁻¹)
2×10^{43}	2×10^{44}	280	3×10^{46}	3×10^{19}	5×10^{22}	2×10^{39}	10^{18}

in its rest frame would be about 20 Jy; signals received at 1 GHz would have been emitted at $\nu = 3$ GHz, and the luminosity $L_\nu = 2.9 \times 10^{17} \text{ W Hz}^{-1}$.

The minimum total energy is

$$W_{\min} \approx 3.0 \times 10^6 \eta^{4/7} (V/\text{m}^3)^{3/7} (\nu/\text{Hz})^{2/7} (L_\nu/\text{W Hz}^{-1})^{4/7} \text{ J} \quad (7)$$

and the associated magnetic field is

$$B_{\min} \approx 1.8 [\eta (L_\nu/\text{W Hz}^{-1}) / (V/\text{m}^3)]^{2/7} (\nu/\text{Hz})^{1/7} \text{ T}. \quad (8)$$

This set of parameters, for one of the radio-emitting components, leads to $W_{\min} = 7.7 \times 10^{35} \text{ J} = 7.7 \times 10^{42} \text{ erg}$ and $B_{\min} = 28 \mu\text{T} = 280 \text{ mG}$.

The Lorentz factor of an electron radiating near 3 GHz is then about 90, and the mean Lorentz factor for this population is 240. (Some authors consider electron distributions that continue to much lower energies, but as yet there is no observational evidence for this. RM99, on the other hand, adopt a higher mean Lorentz factor of 1000, on the basis of a detection of the event at 240 GHz. That emission may well have originated in the inner region of the system; Fig. 4 shows the quasi-periodic oscillations observed at 15 GHz during the early stage of the current outburst which have a flat spectrum (Fender & Pooley 1998) and, with a time-scale of 20 min, must come from a very small region.)

4.1.2 Total number of relativistic electrons

By integrating the electron distribution we can derive an estimate of the total number of relativistic electrons (this may become important if we suppose that each is accompanied by a ‘cold’ proton). This integration requires minimum and maximum energies, but as in the derivation of the total energy the precise value of the upper limit is unimportant; the number is dominated by the low-energy electrons. To establish the constants involved we use equation (19.17) from Longair, which relates the luminosity, the magnetic field and the spectrum, and derive

$$N_{\text{total}} = (L_\nu/\text{W Hz}^{-1}) f(\alpha) / (B_{\min}/\text{T}),$$

where $f(\alpha) = 1.7 \times 10^{24}$ for $\alpha = -0.8$. This results in $N_{\text{total}} = 1.6 \times 10^{46}$.

4.1.3 Kinetic energy

Associated with the bulk motion of the jet there is also the kinetic energy; if the jet contains only e^+e^- plasma and magnetic field, the magnitude of this is $(\gamma - 1) \times W_{\min}$, perhaps $9 \times 10^{36} \text{ J} = 9 \times 10^{43} \text{ erg}$. On the other hand, if the plasma contains cold protons, the kinetic energy will be increased by $(\gamma - 1) \times N_{\text{total}} m_p c^2$. This results in an increase by only a factor of 2. The total of the kinetic energy of the protons could vary, either way, if the conditions were far from ‘minimum energy’, or be substantially larger if the electron energy distribution continues to rise to lower energies, with correspondingly more protons.

We can estimate the power required to produce this injection of energy over 12 h; including the kinetic energy of the system and both sides of the source, we have to generate $2 \times \gamma W_{\min}$ in that time, a power of $2 \times 10^{32} \text{ W}$ or $2 \times 10^{39} \text{ erg s}^{-1}$. Including a similar number of protons approximately doubles that total and also requires a mass-flow rate of $\geq 10^{18} \text{ g s}^{-1}$. X-ray spectral fits (e.g. Belloni et al. 1997b) have been used to derive accretion rates near 10^{18} g s^{-1} .

Many of the observed parameters used here are uncertain, with the dominant effect arising from the unknown distance. Were we to adopt a distance of 9 kpc, the bulk Lorentz factor would be 1.8 rather than 5 and the Doppler factor of the approaching component near 1. Therefore, its flux density in the rest frame would be 1 Jy rather than 20 Jy, and the energy of the system reduced by a factor of about 10.

The results of these calculations of energetics and mass flow are summarized in Table 3 (for a distance of 11 kpc). Indeed, the mass of cold protons could be as much again as in Table 3, if we use the upper limit on electron density ($< 2 \text{ cm}^{-3}$) inferred from Faraday effects discussed in section 3.3.1.

4.2 Comparison with previous major ejections

While it could already be guessed from the higher observed proper motions, our solutions (Table 2, Fig. 6, under the assumption of intrinsic symmetry) illustrate that we cannot avoid deriving a higher velocity for the ejecta than derived by MR94. Thus the two data sets are *not* compatible with a simple change of the angle to the line of sight of a jet that is intrinsically physically identical. In fact, the data *are* marginally consistent with the *same* angle to the line of sight for the jet. The increase in intrinsic β from our observations compared with MR94 is at least 0.05, and more likely ~ 0.1 , corresponding to a significantly higher Lorentz factor for bulk motion by a factor of ≥ 1.3 , as tabulated in Table 2.

It is of great importance to determine whether the different measured velocities are intrinsic to the ejecta or an artefact of the different resolutions of MERLIN and the VLA. In the former case the significantly different measured proper motions could correspond to a difference between the ejection event(s) reported here and the event reported in MR94. The earlier event appears to have been both significantly brighter and to have decayed in flux more slowly. Alternatively, there may be genuine deceleration between the angular scales of up to 300 mas imaged with MERLIN and greater than 400 mas measured with the VLA. This does not seem likely, however, given that both instruments recorded essentially ballistic motions (ignoring the slight apparent curvature) within their multiple observations.

It may be that the different measured proper motions arise from an inability of the VLA to resolve individual components, causing them to blend together in maps. In this case, the VLA could measure lower proper motions and/or apparent decelerations if

- (i) there were multiple components, and

(ii) the components decreased in flux density more rapidly with distance from the core.

This effect is discussed by Hjellming & Rupen (1995) for GRO J1655–40 where they measure apparent decelerations of ~ 30 per cent with the VLA in comparison with VLBA (and SHEVE – Tingay et al. 1995) for two of the three major ejections that they image. Did these effects occur during the observations of MR94? Their maps do indeed show that multiple ejections were occurring during this period (MR94; RM99); and furthermore RM99 discuss evidence that the decay rate of the ejecta increase with angular separation from the core (although they discuss a relatively abrupt increase in decay rate at angular separations ≥ 1 arcsec, which would not have affected the measurements of MR94). So it seems a possibility that the lower measured proper motions arise from blending of multiple components and that the MERLIN measurements more accurately represent the true situation.

In order to test this we have attempted to convolve our MERLIN data with lower resolution beams comparable to that of the VLA observations of MR94. Note that the comparison is not good because of the lack of short baselines in the MERLIN array compared to the VLA. Nevertheless, it was clear from convolution of our data with a 250 mas beam that it was not possible to clearly resolve any individual components. Even with a 100 mas beam, i.e. twice the resolution of the VLA data of MR94, while the approaching and receding sides can be distinguished, individual ejecta on the approaching side cannot.

However, without simultaneous VLA and MERLIN (and possibly also VLBI) observations of the outburst, it is not possible to test this conclusively. So we cannot confidently discriminate between the two most likely explanations, of either intrinsically different velocities between 1994 March/April and 1997 Oct./Nov., or resolution effects between the two arrays. Note that if the latter is the cause of the different measured proper motions then it requires the similar proper motions (range $15 - 18 \text{ mas d}^{-1}$) measured in four instances in 1994 with the VLA (RM99) all to have an origin in similar unresolved multiple ejections. Detailed inspection of radio light curves around these periods may shed some light on this.

The mean position angle of the jet as observed by MERLIN, 142° , is consistent with the range of $140^\circ - 160^\circ$ observed with the VLA (RM99).

4.3 X-ray and radio state at jet formation

GRS 1915+105 offers a unique opportunity to study the jet–disc relation, and in this case we can directly relate changes in the accretion disc X-ray emission to the ejection of significant quantities of material from the system.

Fig. 1 shows the evolving sequence of events as observed by radio and X-ray monitoring of the source. The onset of the plateau phase is preceded by a significant radio flare, similar enough to those mapped by us after the plateau state to interpret it as a major disc ejection.

Almost immediately following this ejection the plateau state is established. It was already known from PF97 that this state, with hard, quasi-steady X-ray emission, corresponded to bright and fairly steady radio emission at 15 GHz. Combination of the RT and GBI data now clearly shows that this state is indeed radio-bright, with a flat or inverted spectral index. This is highly indicative of absorbed emission (although it is conceivable that the electron acceleration mechanism changes to produce a different, optically thin spectrum that mimics absorption), and may suggest the formation of a large optically thick jet. If so, it seems possible

that this may be associated with the infrared jet imaged by Sams, Eckart & Sunyaev (1996). The X-ray emission may also support such a picture, as the soft (disc) component appears to be very weak, if present at all, during this state (Mendez & Belloni, private communication). In addition, no radio oscillations, associated with inner disc instabilities, have been observed during the plateau state.

Fig. 4 shows in more detail the radio and X-ray state of the source at the times of formation of the jets we have imaged with MERLIN. In particular, note the four panels on the right-hand side of Fig. 4, showing the 15-GHz RT monitoring of GRS 1915+105 between MJD 50750 and 50754, i.e. between the first ejection, corresponding to NW+SE, and the second, corresponding to C1. It appears that for the entire period between these two ejections, the inner accretion disc is unstable and material is repeatedly advected and ejected on time-scales of tens of minutes (see Belloni et al. 1997a,b; Fender et al. 1997; PF97; Eikenberry et al. 1998; Mirabel et al. 1998; Fender & Pooley 1998). No such periods of large-amplitude inner-disc instabilities are obvious between subsequent ejections, although the ejection of C2 appears to correspond to a minor X-ray flare, and C3 possibly corresponds to a brief X-ray dip.

5 CONCLUSIONS

Our MERLIN observations have revealed four major relativistic ejections from GRS 1915+105 over a period of approximately two weeks. Over 10 epochs of observation we have consistently measured proper motions of 23.6 ± 0.5 and $10.0 \pm 0.5 \text{ mas d}^{-1}$, for the approaching and receding components, respectively. The proper motion of the approaching component is more than 30 per cent higher than that reported from VLA observations of the source (MR94; RM99). Under the assumption of intrinsic symmetry, we have derived an upper limit for the distance to the system of $11.2 \pm 0.8 \text{ kpc}$. While compatible with the distance of $12.5 \pm 1.5 \text{ kpc}$ quoted by MR94, it seems that the favoured distance to the system should be revised downwards by at least 1 kpc. Solving for the angle to the line of sight and intrinsic velocity, again under the assumption of an intrinsically symmetric ejection, we cannot avoid deriving a significantly higher velocity than MR94, by around $\Delta\beta = 0.1$. We have investigated whether or not the lower resolution of the VLA could result in lower proper motions being measured, as a result of multiple blended components and an increase in decay rate with distance from the core, and this does seem possible. On the other hand, there is no reason to believe that the jet velocity should be fixed – of all the astrophysical objects with relativistic jets, only SS 433 (jet velocity $0.26c$, e.g. Vermeulen et al. 1993) is established to have a constant jet velocity. Further observations at high angular resolutions with MERLIN and/or VLBI, preferably simultaneous with lower resolution VLA observations, will be required to investigate whether there is a systematic deceleration of ejecta on angular scales of ≥ 0.3 arcsec. If MR94 are correct in inferring a large distance for GRS 1915+105 from the column density to the source, then the bulk velocity of the outflow is almost certainly much higher than the currently accepted value of $0.92c$; at 11 kpc we derive $0.98^{+0.02}_{-0.05}c$ at $66^\circ \pm 2^\circ$ to the line of sight.

Our polarization observations clearly reveal rapid evolution of the magnetic field in the ejecta on time-scales of a day or less. This would seem to imply that the region from which the polarized emission arises is smaller than one light day across; consideration of time dilation (stretching intrinsic time-scales when observed in our frame, given our derived solutions for θ and β) only makes this size smaller. The decreasing trend of the polarization with distance from

the core suggests increasing randomisation of the field as the ejecta evolve, although multifrequency polarization measurements are required to rule out or constrain Faraday rotation effects.

As already noted by MR94 and others, the power required for the formation of the jet is immense, far greater than the Eddington luminosity for a solar mass object (at 11 kpc), even without the inclusion of a proton content. Jet formation may well be the dominant power output channel during such periods, and possibly also during periods of smaller oscillation ejections. In addition, when one proton per electron is added the minimum mass flow rate becomes comparable to the mass accretion rates derived from X-ray spectral fits. So, it is possible that during jet formation periods, a significant fraction of the inflowing mass is expelled and does not fall into the black hole. A similar possibility exists for the minor oscillation ejections (Fender & Pooley 1998). Good wavelength coverage of flares to both higher and lower frequencies is required to better determine the luminosity, energy and mass of the ejections. An accurate simultaneous comparison of mass flow through the disc (from X-ray spectral fits) and outflow rates (from radio observations) would be of great interest, to see whether the flows are advection- or ejection-dominated.

Radio and X-ray monitoring of GRS 1915+105 (e.g. Harmon et al. 1997; PF97) had already hinted at a delayed relation between hard X-ray states and radio outbursts. These MERLIN observations have established that these radio outbursts do indeed correspond to relativistic ejections following plateau states. The nature of these states, and the associated inverted-spectrum radio emission is still unclear, and warrants further study. It is also of interest to clarify whether or not the radio flare that *precedes* the plateau state (Fig. 1) also, as expected, corresponds to a major ejection. Why the accretion disc–jet system in GRS 1915+105 appears to switch so rapidly between major mass ejections, short period (oscillation) instabilities and back again (Fig. 4) is still very uncertain. Atayan & Aharonian (1997) discuss the disruption of the accretion disc owing to recoil momentum from an asymmetric ejection. However, it is difficult to reconcile their model with the apparent very rapid reformation of the (unstable) inner accretion disc after the major (NE+SW) ejection. Finally, it is tempting to ascribe the apparent ‘period’ of the jet bending of ~ 7 d to an orbital period, as was found to be the case for GRO J1655–40, but at present this is no more than speculation.

These MERLIN observations are further evidence that GRS 1915+105 repeatedly produces relativistic ejections of massive clouds of synchrotron-emitting electrons. Our observations of very high proper motions in the inner 0.3 arcsec of the jet show that galactic stellar-mass black holes are capable of accelerating matter to velocities very close to the speed of light.

ACKNOWLEDGMENTS

We acknowledge the assistance of many people in the triggering and realization of these observations, including Shane McKie, Richard Ogle and Peter Thomasson. MERLIN is operated as a National Facility by the University of Manchester at the Nuffield Radio Astronomy Laboratories, Jodrell Bank, on behalf of the Particle Physics and Astronomy Research Council (PPARC). We thank the staff at MRAO for maintenance and operation of the Ryle Telescope, which is supported by the PPARC. We also thank the referee for prompt and useful comments. The Green Bank Interferometer is a facility of the National Science Foundation and is currently operated by the National Radio Astronomy Observatory in support of the NASA High Energy Astrophysics programs. Radio

astronomy at the Naval Research Laboratory is supported by the Office of Naval Research. We acknowledge the use of quick-look results provided by the ASM/RXTE team. RPF was supported during the period of this research initially by ASTRON grant 781-76-017 and subsequently by EC Marie Curie Fellowship ERBFMBICT 972436. DJM acknowledges support for his research by the European Commission under TMR-LSF contract No. ERBFMGECT950012.

REFERENCES

- Atayan A. M., Aharonian F. A., 1997, *ApJ*, 490, L149
 Bailyn C. D., Orosz J. A., McClintock J. E., Remillard R. A., 1995, *Nat*, 378, 157
 Bandyopadhyay R., Martini P., Gerard E., Charles P. A., Wagner R. M., Shrader C., Shahbaz T., Mirabel I. F., 1998, *MNRAS*, 295, 623
 Belloni T., Mendez M., King A. R., van der Klis M., van Paradijs J., 1997a, *ApJ*, 479, L145
 Belloni T., Mendez M., King A. R., van der Klis M., van Paradijs J., 1997b, *ApJ*, 488, L109
 Castro-Tirado A., Brandt S., Lund N., 1992, *IAU Circ.* 5590
 Cawthorne T. V., Wardle J. F. C., Roberts D. H., Gabuzda D. C., 1993, *ApJ*, 416, 519
 Downes D., Wilson T. L., Bieging J., Wink J., *A&AS*, 1980, 40, 379
 Eikenberry S. S., Matthews K., Morgan E. H., Remillard R. A., Nelson R. W., 1998, *ApJ*, 494, L61
 Feldt M., Stecklum B., Henning Th., Hayward T. L., Lehmann Th., Klein R., 1998, *A&A*, 339, 759
 Fender R. P., Pooley G. G., Brocksopp C., Newell S. J., 1997, *MNRAS*, 290, L65
 Fender R. P., Pooley G. G., 1998, *MNRAS*, 300, 573
 Foster R. S., Waltman E. B., Tavani M., Harmon B. A., Zhang S. N., Paciesas W. S., Ghigo F. D., 1996, *ApJ*, 467, L81
 Harmon B. A., Deal K. J., Paciesas W. S., Zhang S. N., Robinson C. R., Gerard E., Rodríguez L. F., Mirabel I. F., 1997, *ApJ*, 477, L85
 Harris D. E., Carilli C. L., Perley R. A., 1994, *Nat*, 367, 713
 Hjellming R. M., Rupen M. P., 1995, *Nat*, 375, 464
 Hughes P. A. (ed.), 1991, *Beams and Jets in Astrophysics*. Cambridge University Press, Cambridge
 Kembell A. J., Diamond P. J., Pauliny-Toth I. I. K., 1996, *ApJ*, 464, L55
 Levine A. M., Bradt H., Cui W., Jernigan J. G., Morgan E. H., Remillard R. A., Shirey R., Smith D., 1996, *ApJ*, 469, L33
 Longair M. S., 1994, *High Energy Astrophysics*, Vol. 2, 2nd edn. Cambridge University Press, Cambridge
 Mirabel I. F., Rodríguez L. F., 1994, *Nat*, 371, 46 [MR94]
 Mirabel I. F. et al., 1994, *A&A*, 282, L17
 Mirabel I. F., Rodríguez L. F., Chaty S., Sauvage M., Gerard E., Duc P.-A., Castro-Tirado A., Callanan P., 1996, *ApJ*, 472, L111
 Mirabel I. F., Dhawan V., Chaty S., Rodríguez L. F., Martí J., Robinson C. R., Swank J., Geballe T. R., 1998, *A&A*, 330, L9
 Patnaik A. R., Browne I. W. A., Wilkinson P. N., Wrobel J. M., 1992, *MNRAS*, 254, 655
 Pooley G. G., 1995, *IAU Circ.* 6269
 Pooley G. G., Fender R. P., 1997, *MNRAS*, 292, 925 [PF97]
 Quirrenbach A., Witzel A., Qian S. J., Krichbaum T., Hummel C. A., Alberdi A., 1989, *A&A* 226, L1
 Rodríguez L. F., Gerard E., Mirabel I. F., Gomez Y., Velazquez A., 1995, *ApJS*, 101, 173
 Rodríguez L. F., Mirabel I. F., 1999, *ApJ*, in press [RM99]
 Rupen M. P., Hjellming R. M., Mioduszewski A. J., 1998, *IAU Circ.* 6938
 Sams B., Eckart A., Sunyaev R., 1996, *Nat*, 382, 47
 Tingay S. J. et al., 1995, *Nat*, 374, 141
 Vermeulen R. C., Schilizzi R. T., Spencer R. E., Romney J. D., Fejes J., 1993, *A&A*, 270, 177

This paper has been typeset from a $\mathrm{T}_{\mathrm{E}}\mathrm{X}/\mathrm{L}^{\mathrm{A}}\mathrm{T}_{\mathrm{E}}\mathrm{X}$ file prepared by the author.